

Provided for non-commercial research and education use.  
Not for reproduction, distribution or commercial use.

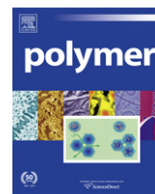


This article appeared in a journal published by Elsevier. The attached copy is furnished to the author for internal non-commercial research and education use, including for instruction at the authors institution and sharing with colleagues.

Other uses, including reproduction and distribution, or selling or licensing copies, or posting to personal, institutional or third party websites are prohibited.

In most cases authors are permitted to post their version of the article (e.g. in Word or Tex form) to their personal website or institutional repository. Authors requiring further information regarding Elsevier's archiving and manuscript policies are encouraged to visit:

<http://www.elsevier.com/copyright>



## Strain-induced internal fibrillation in looped aramid filaments

Brian R. Pauw<sup>a,b,\*</sup>, Martin E. Vigild<sup>a</sup>, Kell Mortensen<sup>c</sup>, Jens W. Andreasen<sup>b</sup>, Enno A. Klop<sup>d</sup>,  
Dag W. Breiby<sup>e</sup>, Oliver Bunk<sup>f</sup>

<sup>a</sup>Danish Polymer Centre, Department of Chemical Engineering, Technical University of Denmark, Langelandsgade 140, DK-2800 Kgs. Lyngby, Denmark

<sup>b</sup>Solar Energy Programme, Risø National Laboratory for Sustainable Energy, Technical University of Denmark, P.O. 49, DK-4000 Roskilde, Denmark

<sup>c</sup>Department of Basic Sciences and Environment, Faculty of Life Sciences, University of Copenhagen, 1871 Frederiksberg C, Denmark

<sup>d</sup>Teijin Aramid BV, Research Institute, Dept. QRS, P.O. Box 5153, 6802 ED Arnhem, The Netherlands

<sup>e</sup>Department of Physics, Norwegian University of Science and Technology, Høgskoleringen 5, N-7491 Trondheim, Norway

<sup>f</sup>Paul Scherrer Institut, Swiss Light Source, 5232 Villigen PSI, Switzerland

### ARTICLE INFO

#### Article history:

Received 22 April 2010

Accepted 28 July 2010

Available online 5 August 2010

#### Keywords:

PPTA

SAXS

Strain

### ABSTRACT

By mapping the small-angle X-ray scattering (SAXS) from a looped poly-(*para*-phenylene terephthalamide) (aramid, PPTA) filament using a synchrotron X-ray microbeam, we investigate the effects of axially compressive and tensile strain on internal fibrillar structures. Unique observations of oscillations in the highly anisotropic SAXS patterns indicate a regular internal structure. Upon increase of the applied compressive strain, a significant decrease in oscillation frequency is observed in the scattering pattern. With an increase in imposed tensile strain an increase in oscillation frequency in the scattering pattern is observed. One model capable of describing the intensity is a model of stacked cylinders. These cylinders could be part of the fibrillar structure present in the PPTA fibres, which consist of cylinder- to tape-like objects, the presence of which is supported by SEM images. One hypothetical physical interpretation presented here for the appearance of a regular internal structure is the occurrence of fibrillar separation in regions undergoing axially compressive strain, and the appearance of strain relief/slip planes between packs of fibrils in regions undergoing tensile strain. Compaction of these packs upon increase of tensile strain could increase the repetition distance in the structure as multiple packs combine to form a single pack.

© 2010 Elsevier Ltd. All rights reserved.

### 1. Introduction

High-performance fibres are produced by extruding polymer into a large number of polymer filaments, thus forming fibre yarns. It is well known that during this process, nanostructures tend to form within the individual filaments (the diameter of one filament is approximately 12  $\mu\text{m}$ ) [1]. Investigations show a strong correlation between the properties of the nanostructure and the physical properties of the fibres [2–4]. High-performance polymer fibres, such as poly-(*para*-phenylene terephthalamide) (PPTA) fibres, commercialized as Twaron and Kevlar (trademarks of Teijin Aramid and DuPont, respectively), are examples of fibres exhibiting such a nanostructure in its constituent filaments [4]. One of the nanostructural building blocks is the fibril. In aramid filaments, fibrils

are elements that pack into superstructures, sometimes referred to as “macrofibrils”. Each of the fibrils, in turn, consists of a large amount of “microfibrils” [5].

In addition to this structure there is considerable evidence for the presence of a nanoporous structure in the filaments [1,4,6–9]. Firstly, there is the difference between the crystalline density of PPTA (1.48  $\text{g cm}^{-3}$ ) and the macroscopic density of the material (which ranges from 1.45 to 1.47, depending on the production process [1,4,10]). The absence of an amorphous diffraction signal indicates that little or no amorphous PPTA is present, so that the reduced density is likely to be due to about 5 vol% of voids. Furthermore, direct observations of a porous structure have been obtained through transmission electron microscopy by (amongst others) Dobb et al. [11]. In other investigations the moisture uptake in the filaments is analysed. The moisture is partially transported through and stored in a void structure [8,6]. Finally, the presence of a strong Small-angle X-ray Scattering (SAXS) signal strongly supports the presence of voids, especially since it is dependent on the moisture content [11,8]. The void structure appears analogous to that found in carbon fibres [12], although it exhibits a lower aspect

\* Corresponding author. Danish Polymer Centre, Department of Chemical Engineering, Technical University of Denmark, Langelandsgade 140, DK-2800 Kgs. Lyngby, Denmark. Tel.: +45 45256801.

E-mail address: [brian@stack.nl](mailto:brian@stack.nl) (B.R. Pauw).

ratio [1]. An alternative explanation for the existence of the SAXS signal is that this signal could also originate from an amorphous phase instead of a void structure [13,14]. Ran et al. [13] reached this conclusion partially since they did not observe a change in the SAXS pattern when subjecting PPTA fibres to moisture. In view of the investigations referred to above, it is at present commonly accepted that a void system is present in the fibres.

Small-Angle X-ray Scattering (SAXS) is well suited to characterise structures ranging from approximately 1 nm–1  $\mu\text{m}$ , the results of which are invaluable for establishing structure–property relationships. Microfocused X-ray sources, such as the cSAXS beamline at the Swiss Light Source, allow local probing of the structure inside single filaments. The filament diameter of the Twaron studied in this work is typically around 12  $\mu\text{m}$ , and the cSAXS beamline has a beam with a cross-section of 4 microns in the smallest dimension, thus allowing the local fibrillar structure to be probed.

Local probing is particularly valuable when the filament is exposed to local perturbations, such as bending or stretching. Understanding the filament structural response to bending is essential to the successful use of fibres in applications, as bending causes compressive, shear and tensile forces in the filaments which eventually leads to failure (cf. Fig. 1). In aramid high-performance polymers the compressive stress at failure is about 20% of the tensile stress at failure.

Bending failure modes of filaments can generally be classified into tensile failure and kink band formation. Tensile failure occurs with brittle fibres such as glass fibres and carbon fibres, whereas kink band formation occurs mainly in polymer fibres [15]. The latter bending failure mode may be due to Euler buckling, which is expressed as kinks on the surface of the filament, starting from the compressed area of the filaments [16,17]. Raman spectroscopy has shown that at these kink bands, the strain in the fibre is reduced [18].

One method to control bending is to force the filament into a loop, a method known as the “elastica loop test” (cf. Fig. 1) [15]. The strain in the sample can then be calculated from the radius of curvature, which is smallest at the apex of the loop, corresponding to the highest strain. In elastic deformation, the zero-strain point occupies the centre of the filament, but will shift as soon as non-elastic deformation takes place. A similar recent experiment shows that bending (of carbon fibres) introduces a strain in the sample, with the zero-strain point close to, but not necessarily exactly at the centre of the filament [19].

In the present study, microfocused SAXS was used for in-situ monitoring of loop deformation, using the elastica loop test with a custom-made “loop device”. From the scattering pattern we were able to establish the evolution of fibrillar separation in regions with an imposed axially compressive strain, and fibrillar compaction in regions with an imposed tensile strain.

## 2. Experimental

### 2.1. Sample preparation

The sample consists of a filament of as spun poly-(*para*-phenylene terephthalamide) (PPTA, a precursor to commercially available Twaron), 12  $\mu\text{m}$  in diameter, spun from a liquid crystalline solution of PPTA in sulfuric acid. The filaments have not undergone a heat treatment procedure after the washing and drying steps. The heat treatment procedure is commonly applied to commercially available filaments to optimize the physical properties.

All samples for the SAXS studies were prepared one week before the scattering experiments, and allowed to dry in vacuum before transportation to the SAXS beamline in a box kept dry with silica gel. Upon arrival at the synchrotron, the samples were subjected to a further 12 h of vacuum drying before being stored in a box with

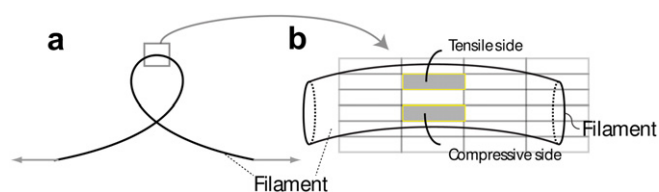


**Fig. 1.** a) The elastica loop experiment, and b) the apex (top) of the loop, where regions under stress are indicated. The size of the shaded areas corresponds to the size of the X-ray beam available at the cSAXS beamline, showing that three to five non-overlapping measurements can be made across the filament diameter.

desiccant. The samples were handled carefully to ensure no damage prior to the bending experiments.

### 2.2. Scanning electron microscopy

Scanning Electron Microscopy (SEM) experiments were performed at the Center for Electron Nanoscopy at the Technical University of Denmark (DTU), using a FEI Quanta 200F, operated with an electron acceleration voltage of 2 keV, a spot size of 2.0 nm, and a working distance of 4.5 mm.

### 2.3. SAXS measurements

The SAXS experiments were carried out at the coherent SAXS (cSAXS, X12SA) beamline of the Swiss Light Source, using a monochromatic beam with a wavelength of 0.100 nm. The scattered X-rays were collected using a two-dimensional detector, specifically a Pilatus 2 M, with a pixel size of  $172 \times 172 \mu\text{m}^2$  and a total of  $1461 \times 1560$  pixels [20]. The detector area consists of 24 rectangular modules, mounted in a  $3 \times 8$  arrangement, with small gaps between the modules. This detector was pivotal to the success of the experiment, as it has no electronic (background) noise and a pixel-limited point spread function. Typical exposure times were 1 s per frame, with a read-out time of 5 ms. A 7 m helium-filled flight-tube spanned the flight path between the sample and the detector. The sample was kept in air during the measurements. Alignment was facilitated by a remotely controlled optical microscope, which was also used to monitor and measure the loop width and height. The beam was focused using the second monochromator crystal and a Rhodium-coated mirror to a rectangular cross-section of  $20 \times 4 \mu\text{m}^2$  ( $h \times v$ , FWHM) at the sample position. The PPTA filaments were sequentially measured with the filament axis oriented parallel to the main axis of the (20  $\mu\text{m}$  wide) cross-section of the focused beam (as visualized in Fig. 1).

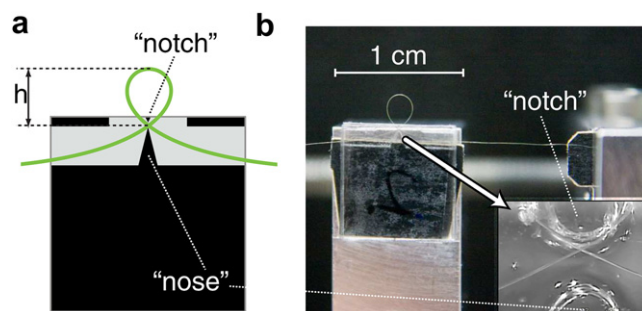


**Fig. 2.** The elastica loop contained within the microchannel device is shown in a), with the loop height  $h$ , “notch” and “nose” structures indicated (the filament thickness is exaggerated for clarity). b) shows the loop device as installed at the SLS, mounted on the motorized stretching device. The inset in b) shows the filament cross-over point contained in between the “notch” and “nose” structure of the microchannel device.

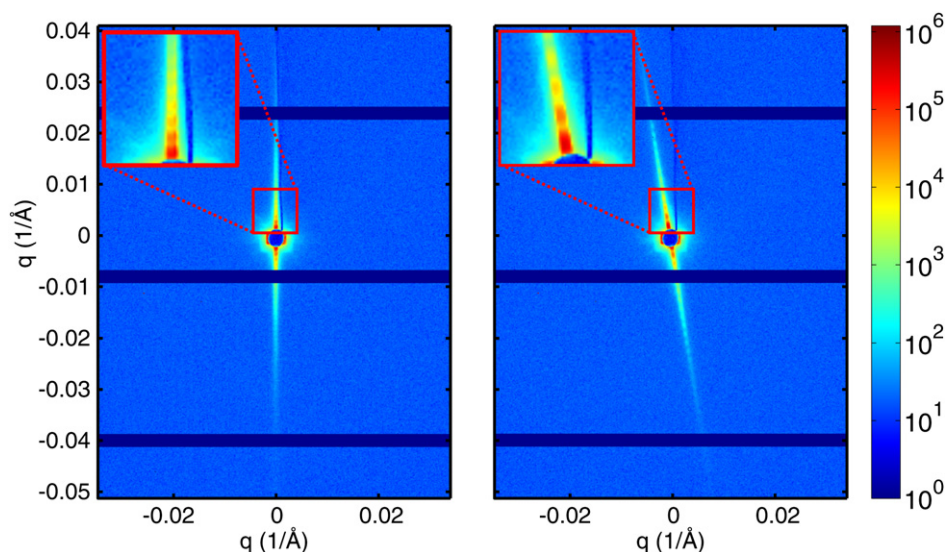


**Fig. 3.** A selected region of the total detector output on a logarithmic intensity scale for two measurements through the looped PPTA filament, showing the highly anisotropic scattering pattern, the beamstop and the gaps between the detector modules. The main axis of the scattering pattern on the left is vertical ( $\psi = 90^\circ$ ), indicating that the measurement was done on a horizontal part (top) of the looped filament, whereas the measurement on the right was performed slightly offset from the apex of the loop. Oscillations in intensity are visible in the insets.

The measurements were carried out as mesh scans, where sequential exposures were made after small translations of the sample (typically about 25 microns horizontally, and 5 microns vertically), thus obtaining a “map” of the scattering from different parts of the filament. For each iteration, the loop diameter was reduced, its new size and shape determined by on-line optical microscopy and a new SAXS map was measured. The full duration of all the measurements on one filament typically lasted several hours.

#### 2.4. Loop device

For the bending experiments, a custom sample holder was made to meet two criteria: the filament should be kept in a size adjustable loop, and the filament should be accessible for X-ray transmission measurements. A microchannel device to guide the filament and contain the cross-over point was constructed out of sandwiched poly(methyl methacrylate) (PMMA) plates. The bottom plate contains a structure shown in Fig. 2 (inset) embossed using a CO<sub>2</sub> laser, with a channel depth of approximately 100 microns. The top piece was subsequently attached to the bottom plate by curing under load at 90 °C for 30 min.

When loading the microchannel device with the filament, care was taken not to damage the filament section that was to be measured. Both ends of the filaments were clamped to a spindle with reversed threads, designed to pull the filament ends apart at equal speed. This increases the strain in the whole loop, and in particular at the apex where the radius of curvature is the smallest. The spindle is driven by a stepper motor, and the sample holder and mounted filament are visible in Fig. 2. During the experiment the cross-over point of the filament is kept in position by the small “notch” and “nose” structures. The filament moves without visible effort through the device, i.e. no “jumps” or other sudden motions are observed during operation, indicating a smooth motion of the filament through the device.

#### 2.5. Data reduction

All data reduction is performed using custom-built functions in the Matlab environment. The detector pixels are indexed in terms of momentum transfer  $q$  and angle  $\psi$ , where  $q$  is defined as  $q = \lambda^{-1} 4\pi \sin \theta$  with  $\lambda$  the wavelength, and  $2\theta$  the scattering angle.

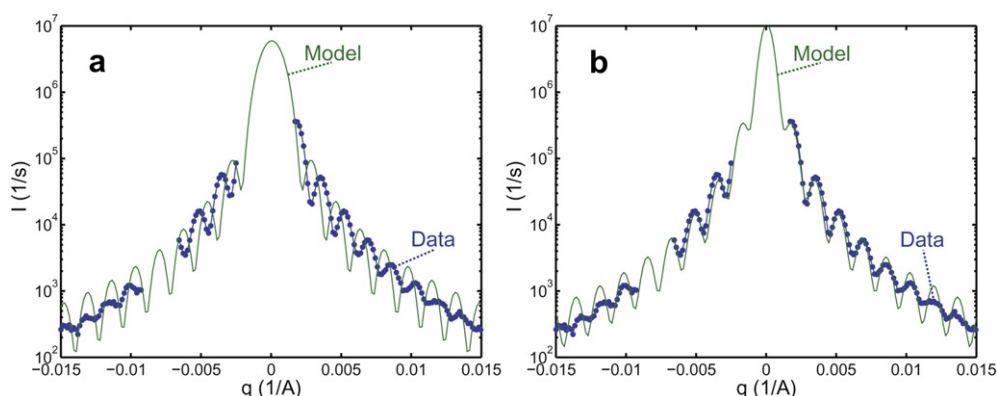


**Fig. 4.** 1D scattering plot obtained from the compressive side of a 7.70 mm high loop (intermittent line with data points indicated), fitted to: a) a cylinder scattering function (continuous line) of a single, perfectly oriented cylinder with a radius of 184.8 nm, and b) the scattered intensity of packed cylinders (continuous line) for cylinders with a spacing of 369.6 nm. The two gaps in the data set originate from the beamstop (centre gap) and a gap between detector modules (left-hand gap).

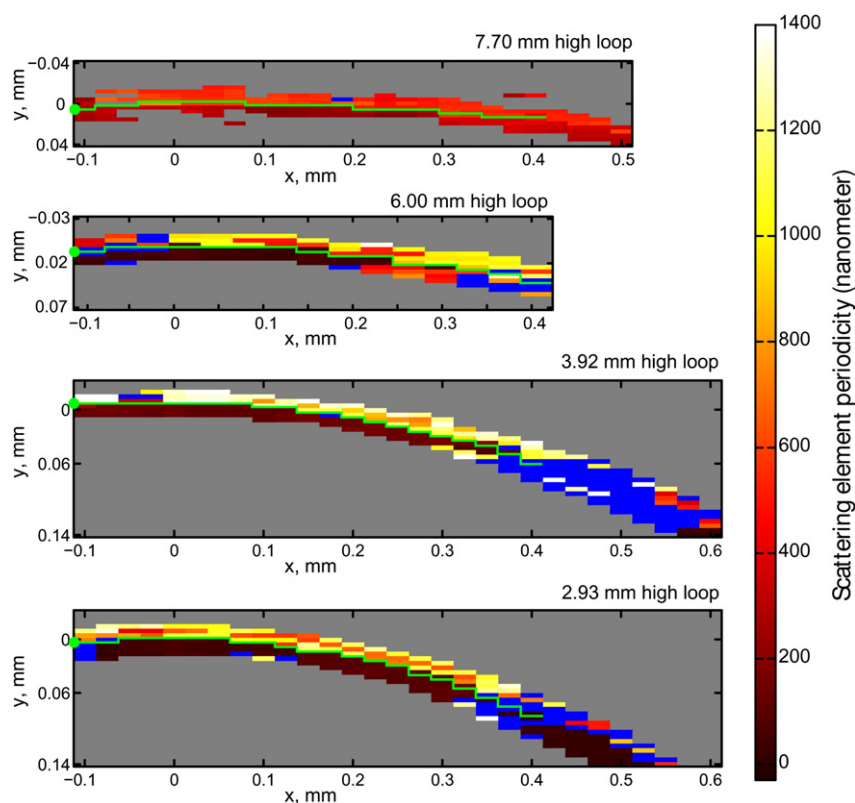


**Fig. 5.** Maps of the scatterer spacings generated from the SAXS data. The horizontal and vertical axis units are in millimeters, colour axis units depict the spacing (in nm) between the cylinder centres that was used to fit the oscillations in the extracted 1D plot. The blue colour indicates regions where no clear oscillations were seen. The green line, halfway between the top and bottom of the filament, indicates the separation boundary between regions of compressive and tensile strain. (For interpretation of the references to colour in this figure legend, the reader is referred to the web version of this article.)

$\psi$  is the polar angle in the detector plane. As the scattering is confined to a sharp line of oscillations on the detector, cf. Fig. 3, a line is extracted along a direction of  $\psi$  of maximum scattered intensity using a Bresenham line extraction algorithm.

A least squares minimization function is used for the fitting, with logarithms of the intensities to increase the relative weight of the low intensity data points. Information on the characteristic lengths in the structure is extracted by fitting the data with a model of infinitely long, stacked cylinders (or aligned ellipsoidal tapes). Details of this can be found in Appendix A.

### 3. Results and discussion

The SAXS scattering patterns obtained from looped as spun PPTA samples show pronounced periodic intensity oscillations at most measuring points, indicating the presence of relatively monodisperse objects and/or a periodic structure in the filament (see, for example, Fig. 4). These oscillations are not commonly observed in straight, unstrained filaments (not shown), nor are they seen in looped heat-treated samples (i.e. filaments of commercially available Twaron, to which the as spun, non heat-treated material

can be considered as a precursor). Heat treatment affects the crystallite size in PPTA [21], and may be related to the disappearance of oscillations in the structure.

Observation of these oscillations was unexpected, but the following consideration of instrumental sources or other artefacts gives us confidence that the scattering originates from the sample. The orientation of the streak-shaped scattering pattern being perpendicular to the fibre axis indicates that the scattering originates from the sample. The periodicity is furthermore indicative of a structure at least an order of magnitude smaller than the beam dimension and correlation volume, and two orders of magnitude smaller than the dimension of the sample, making surface scattering effects unlikely. A well-defined skin layer could also cause oscillations to appear, however, this would scatter as an isolated lamellar structure and be visible only when illuminating the edges of the filament, and not when measuring through the core of the filament.

The period of the oscillations indicates a structure with a characteristic dimension of approximately 100–600 nm. The high anisotropy indicates almost infinitely long objects in the fibre direction. The intensity decay follows a  $q^{-3}$  slope, which suggests a cylindrical structure. The presence of crack formation or local

**Table 1**  
Tabulation of the loop parameter and fitting results.

Loop height (mm)	Radius of curvature (mm)	Max. Strain (%)	Comp. side mean spacing (nm)	Comp. side std. dev.	Tensile side mean spacing (nm)	Tensile side std. dev.
7.70	2.97	0.40	366	127	562	81
6.00	2.27	0.53	282	302	838	290
3.92	1.43	0.84	252	270	1144	312
2.93	1.05	1.10	167	236	900	308

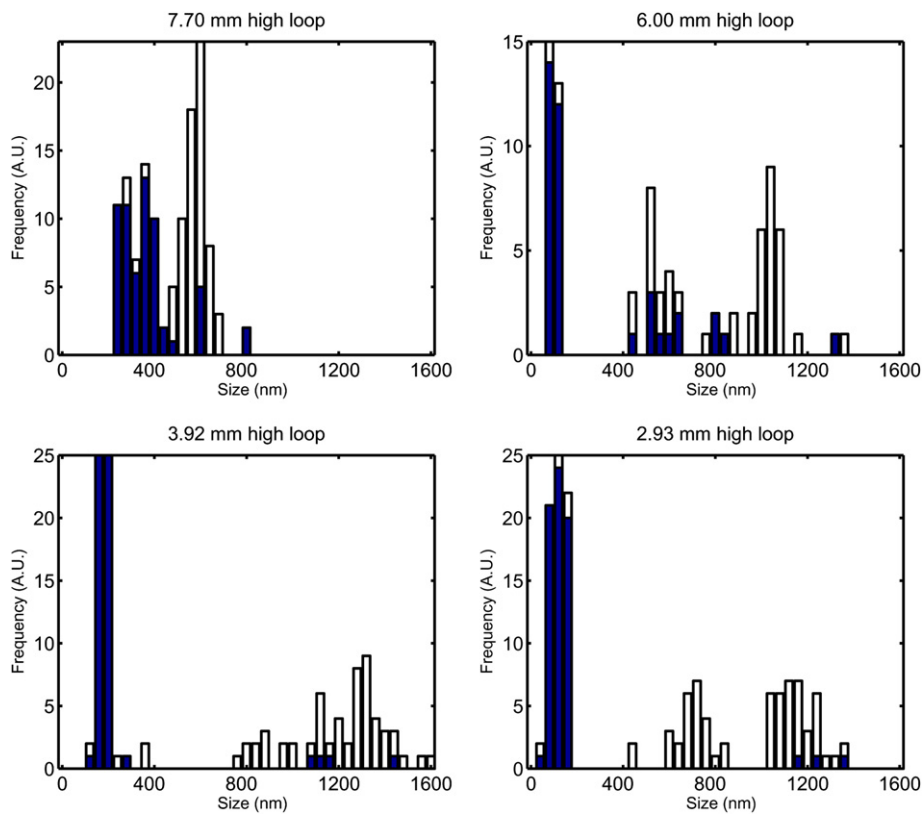


Fig. 6. Size histograms for the compressive (dark) and tensile (white) sections of the loops.

fibril failure in the samples could result in isolated cylinder-shaped voids, but a fit of the data to the form factor of a single cylinder [22], however, shows an offset of the oscillations (Fig. 4), whilst the period matches. Attempts to fit scattering functions of other isolated shapes within the superellipsoid family also did not result in a satisfactory agreement.

The simplest possible model that approaches the scattering behaviour found in the sample is a model consisting of stacked cylinders (stacked in the direction perpendicular to the beam in the plane of bending). The stacking introduces Bragg scattering at positions that coincide with the oscillation positions in the scattering pattern. This packing has a periodicity identical to the

diameter of the cylindrical scatterers, while the cylinder form factor ensures a  $q^{-3}$  dependency of the intensity. This model is shown compared to the data in Fig. 4. The important factors effecting the oscillations in intensity are not the size of the scatterers but the periodicity and shape of the scatterers. In other words, the scattering profiles should be roughly cylindrical in shape, do not need to be monodisperse, but their centres should be positioned at regular intervals. It is this spacing that determines the period of the oscillations, and the shape determines the slope. Additionally, the shape does not need to be cylindrical with a circular cross-section, but can also have an ellipsoidal cross-section (i.e. tape-like objects), which will result in the same scattering pattern as long as the

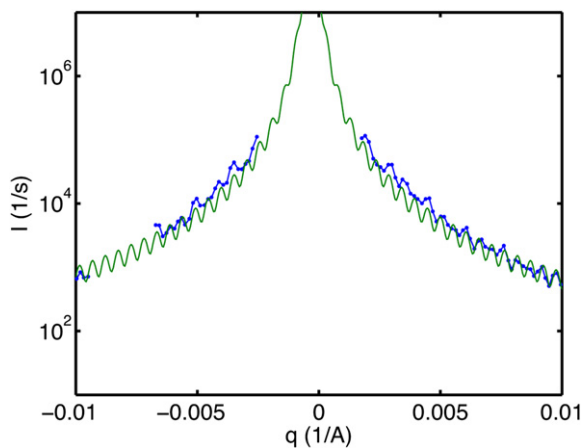


Fig. 7. Scattering pattern obtained from the tensile side of the 1.43 mm high loop, where the oscillations indicate a structure with a periodicity of about 800 nm.

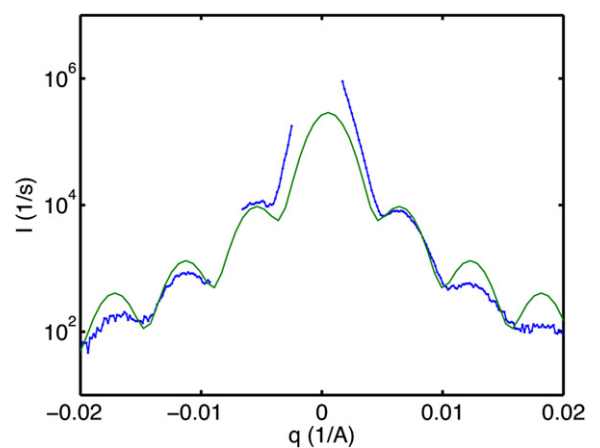
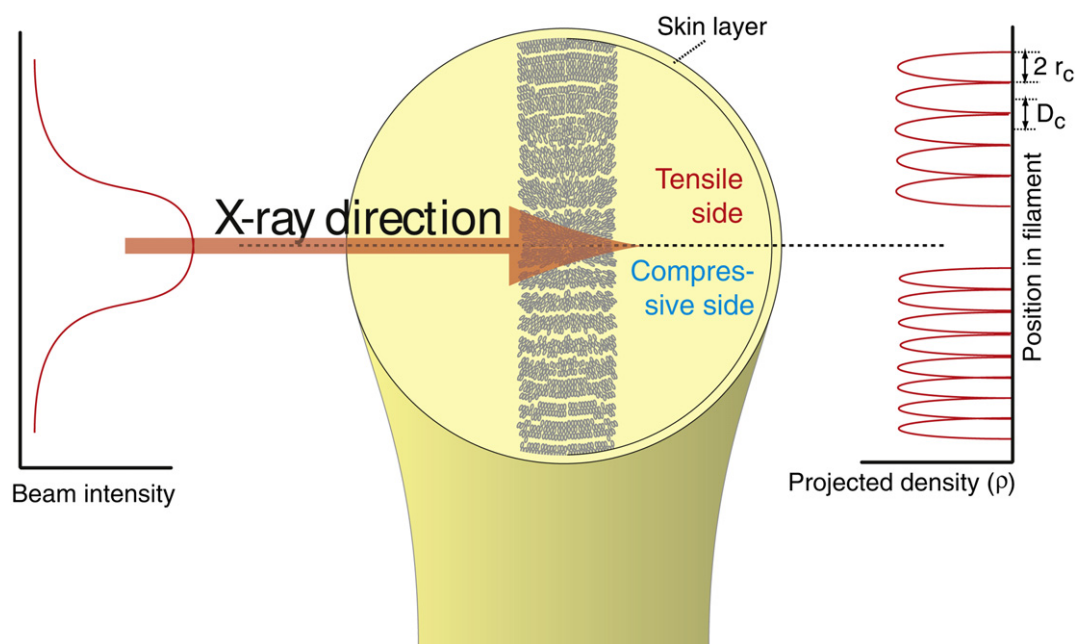


Fig. 8. Scattering pattern obtained from the compressive side of the 1.05 mm high loop, where the oscillations indicate a structure with a periodicity of about 100 nm.



**Fig. 9.** Artist's impression of the cross-section of the looped filament, showing packing of fibrils in the tensile side, and fibrillar separation occurring in the compressive side. The projected electron density is shown on the right-hand side, showing cylindrical profiles with radii of approximately 250 nm (and a spacing  $D_c$  of 500 nm) on the compressive side and 400 nm ( $D_c$  800 nm) on the tensile side.

minor axis is either parallel or orthogonal to the beam (i.e. a stack of tape-structures would give the same scattering (albeit a different total intensity) as a stack of cylinders).

The dampening of the oscillations in the data at higher  $q$  can be modelled as an effect of polydispersity in cylinder spacing, and it was found that considerable polydispersity in the spacing is allowed before the oscillations dampen out. Other aspects that play a role in the analysis is the limited beam width which limits the number of cylinders that are irradiated depending on the size of the cylinders and the spacing between the cylindrical scatterers. While we found that the period and offset of the oscillations is not affected in calculations of a pack consisting of a reduced number of cylinders for this experiment, it will be prudent for experiments using smaller beam widths to more accurately model the beam profile.

With this model, we can characterise the periodicity of the structure that is required to bring about the oscillatory behaviour of the intensity, and some preliminary conclusions regarding the structure in the sample can be made.

An analysis of all obtained scattering patterns with this model allows the generation of a map of the found spacings between the structures effecting the oscillations, which is shown in Fig. 5. The observations in that map include the following (which is also tabulated in Table 1 and shown in a histogram in Fig. 6): The 7.70 mm loop exhibits pronounced oscillations. On the tensile (outer) side of the loop, we find oscillations caused by packed structures with spacings of approximately 600 nm. On the compressive side, these spacings are about 360 nm. The right side of the map shows intermediate spacings of about 500 nm. The tensile and compressive regions appear to be well separated. The “zero”-strain region appears to be located nearby the centre of the filament. There is one region (indicated in blue) where the scattering pattern did not exhibit clear oscillatory behaviour.

Tightening of the loop further enhances the clear separation of the observed domain sizes in the loop, with the spacings in the tensile side approaching 840 nm whereas the spacings in the compressive side are reduced to about 280 nm in size. The high

frequencies in  $I(q)$  become challenging to fit, as the period of the oscillations approaches the pixel size, corresponding to a maximum measurable spacing of about 2000 nm for that detector. Additionally, the pixel width effectively forms bins, reducing the visibility of the oscillations. Therefore, moiré-like effects in combination with the pixel size reduce the accuracy of the determination at higher frequency (larger radii) (see for example Fig. 7).

Further tightening of the loop shows the spacing in the tensile section approaching 1140 nm (c.f. Fig. 7), while on the compressive side, the spacing shows a reduction to approximately 240 nm.

The smallest loops tend to exhibit less pronounced oscillations. The tensile side mean spacing remains stable at around 900 nm, and compressive side spacings are about 160 nm (c.f. Fig. 8). All of the results are tabulated in Table 1.

The overall trend is that upon the application of tensile strain, there is a slight increase in scattered intensity (c.f. Appendix C), while the spacing between the scattering elements increases initially from about 300 nm for the 7.7 mm high loop, to approximately 500 nm for the 2.93 mm loop, and remains there for the duration of the experiment. On the compressive side, the scattering intensity increases more than in the tensile section (c.f. Appendix C), and the spacings between the scattering elements are continuously reduced from 500 nm to less than 200 nm.

One hypothetical structural model that could account for such behaviour is by considering each macrofibril inside the filament to be a packing of smaller fibrils. Upon bending, the strain upon the macrofibril causes it to split into its component fibrils along crack planes, perpendicular to the plane of the loop. On the compressive side, an increasing number of cracks and splits causes the apparent size to reduce. This is supported by observations by Greenwood and Rose, who made observations that kink band formation is related to fibrillar separation in axially compressed fibres [23]. This fibrillar separation results in an improved contrast in the projected electron density profile and thus a higher scattered intensity. On the tensile side, sets of fibrils are packed tightly together, so that virtually no interfibrillar space exists (i.e. boundaries disappear), apart from strain relief planes, and the packs of fibrils scatter as a single element. This would

significantly increase the periodicity (spacing) between the scatterer centres. These effects are conceptually drawn in Fig. 9.

In this artist's impression, several aspects of the internal structure have to be consolidated. Firstly, the structure in the SEM micrographs (c.f. Appendix B) indicates a tape-like fibrillar structure underneath a smoother skin layer. Others have indicated the presence of a radial texture present in PPTA filaments [24–26], which may also be present. Finally, in order to achieve the structure required for obtaining the scattering pattern, at least part of the structure must show periodic interfaces perpendicular to the plane of the loop. These periodic interfaces are indicative of strain relief effects caused by the axial strain gradient present. Differences in periodicity between the tensile side and compressive side may indicate a different method for tensile and compressive stress relief at those sides. At the compressive side, there is evidence for fibrillar separation, at the tensile side, these may be slip planes.

Further experiments are required to elucidate the exact cause for the appearance of these oscillations. A smaller beam size would be preferred, with a lower limit of one micron (as the beam has to remain larger than the scatterers we wish to observe). Rotation of the bent filament with respect to the incoming beam should reveal more about the directionality, shape and rotation of the scattering objects. An in vacuum sample chamber would reduce the background scattering and moisture uptake in the sample. Lastly, in-situ WAXS experiments can act as a local probe for the strain on the crystallites, as their reflection positions have been observed to be dependent on the strain [27]. Initial measurements obtained from the BW2 beamline at HASYLAB, however, show no visible effect of this strain on the diffraction peaks, supporting the notion of a strain relief mechanism.

#### 4. Conclusions

To conclude, filaments of as spun PPTA material contain a packing of fibrils which is easily observed using SEM. These fibrils appear to have a cylinder- to tape-like shape with varying cross-section aspect ratios. The results obtained from microbeam SAXS experiments indicate that in this material (which has not undergone heat treatment under tension), fibrillar separation can occur at bending radii smaller than several millimeters. This fibrillar separation process appears at the compressive side as a reduction in overall fibril spacing upon an increase in axially compressive strain. On the tensile side, there appears to be a fibrillar compaction (packing), where a clear increase in apparent fibrillar spacing results from the imposed strain, likely caused by the disappearing of interfibrillar boundaries due to the compaction. Whilst the onset of these processes was not observed, it is clear that they must occur at bending radii of several millimeters, as oscillations were not observed in straight filament sections. The fact that oscillations were not observed for heat treated filaments indicates that the heat treatment procedure significantly affects this quite remarkable fibrillar structure.

#### Acknowledgements

The authors thank Thomas W. Hansen at the DTU Center for Electron Nanoscopy for his work on obtaining the electron micrographs. They furthermore thank Jörg Vogel at DTU Nanotech for his work on the laser embossing of the microchannel device. The Paul Scherrer Institute in Switzerland is acknowledged for beamtime at the cSAXS instruments of the SLS. This work was supported by the Danish Centre for the use of Synchrotron X-Ray and Neutron Facilities (DANSCATT) sponsored by the Danish Research Council for Nature and Universe. D.W. Breiby also wishes to thank the Norwegian Research Council for financial support.

#### Appendix A. Data reduction details

A least squares minimization function was used for the fitting, with logarithms of the intensities to increase the relative weight of the low intensity data points, i.e.:

$$\chi^2 = \frac{\sum (\log(I_{\text{calc}}) - \log(I_{\text{obs}}))^2}{N - n_{\text{fitparam}}} \quad (\text{A.1})$$

here,  $\chi^2$  is the minimization parameter,  $N$  the number of data points,  $n_{\text{fitparam}}$  the number of variables of the fitting function,  $I_{\text{calc}}$  the calculated (model-)intensity and  $I_{\text{obs}}$  the observed intensity.

A number of models have been tried in an attempt to fit the experimental data. One model capable of describing the experimental data is a numerical model of packed cylinders<sup>1</sup>. A projection of the electron density profile of a cylindrical cross-section onto a line was used as a basis. Rewriting the Cartesian circular cross-section, we obtain for the projected electron density  $\rho(x)$ ,

$$\rho(x) = \sqrt{1 - \left(\frac{x}{r_c}\right)^2} \quad (\text{A.2})$$

where  $r_c$  is the radius of the cross-section in Å. In order to mimic a tightly packed 1D array of cylinders, the profile is replicated by placing copies of itself at a distance of  $2r_c$  to generate  $\rho(x)_{\text{packed}}$ . The spacing between the cylinder centres (periodicity) is therefore  $D_c = 2r_c$ . The cylinders are replicated 10 times to numerically approximate a packed array limited by the width of the beam. The main features of the scattering pattern become independent of the number of replications when this number increases beyond  $n \approx 3$ . The entire line was quantized using  $1 \times 10^4$  points, so that each cylinder in the 10-cylinder model is described using 1000 points (cf. Fig. A.10).

The scattered intensity from this profile is proportional to the absolute square of the Fourier transform of the electron density contrast [28], i.e.:

$$I(q) = \left| \text{FT}(\rho(x)_{\text{packed}}) \right|^2 \quad (\text{A.3})$$

with FT indicating a one-dimensional Fourier Transform. The intensity decay at higher angles obtained from such numerical computations can be improved slightly by convoluting the intensity with the Fourier transform of a box function with the width of the distance between the sampling points. This procedure reduces the error introduced by the discrete Fourier transform, as is explained in detail by Schmidt-Rohr et al. [29]. Finally, effects such as beam profile, polydispersity and graded interfaces are modelled by convoluting the intensity with a single Gaussian, since our main interest lies in the determination of the spacing between the scatterers. The width of this Gaussian depends on the size of the scatterers. For small scatterer sizes of about 50–100 nm (corresponding to spacings of 100–200 nm), the smearing width was set to  $\approx 0.001 \text{ \AA}^{-1}$ , and for scatterers with large sizes (i.e.  $\leq 200 \text{ nm}$ ,  $D_c = 400 \text{ nm}$ ) it was set to  $\approx 1.5 \times 10^{-4} \text{ \AA}^{-1}$ .

#### Appendix B. Scanning electron microscopy

Fig. B.11 shows a SEM micrograph obtained from a loop of as spun material, where part of the skin layer has delaminated. In Fig. B.12, the inner structure is shown in a filament which was cut using scissors. In the first of the obtained SEM micrographs, a fibrillar

<sup>1</sup> The numerical model is chosen over an analytical model for its flexibility in shape and packing of the scatterers. With this model the effect of a large number of structural modifications on the scattering pattern can and has been explored.

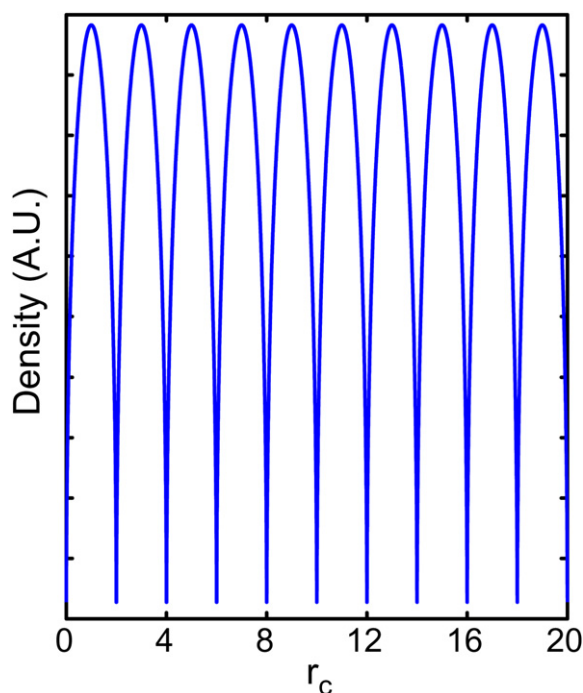


**Fig. A.10.** The projected (electron) density profile  $\rho(x)_{\text{packed}}$ , corresponding to a close packed array of ten cylinders with cylinder radii of 200 nm and a spacing of 400 nm, spanning the approximate width of the beam.

structure can be observed lying underneath the skin of the filament (Fig. B.11). The dimensions of these fibrils are about one hundred nanometers (Fig. B.12), whereas the filament diameter is approximately 12  $\mu\text{m}$ . The skin in this sample is partially delaminated from the bulk of the filament. The outside of the filament is much less rough than the fibrillar structure lying underneath. In some micrographs, a pronounced ribbon or tape-like fibrillar shape is observed throughout the filament (Fig. B.12), with a high aspect ratio ( $\approx 2\text{--}10$ ) of the cross-section. In other micrographs the fibrils appear to have a more circular cross-section.

### Appendix C. Analysis of the scattered intensity

Intensity maps were generated by plotting the integrated intensity (over the extracted line) of all measurements of a loop onto a grid to create a scattered intensity “image” of the object. Compared to integrating over the entire detector area, this procedure yields a better signal-to-noise ratio.

Mesh scans through the loop are analysed using the method described in the data reduction section, yielding values for the intensity (and rotation angle) of the scattering pattern. Obtained intensity maps are shown in Fig. C.13. Here, maps are shown for one loop of as spun PPTA at four different strain levels (i.e. loop sizes). The heights of the loop (measured from the cross-over point to the apex of the loop, indicated as  $h$  in Fig. 2) are 7.70, 6.00, 3.92 and 2.93 mm. From the simultaneously recorded microscopy images of the loop it was verified that the loop did not shift laterally or rotate during the experiment.

The intensity maps reveal a significant increase in intensity as the loop is pulled smaller. In the loops of smaller diameter, the intensity tends to concentrate near the compressive (inner) side of the apex of the loop. Bending did not have a discernible effect on the degree of anisotropy in the scattering pattern, which remained a sharp line during the experiments. It is therefore unlikely that the increased scattered intensity can be attributed to a strain-induced

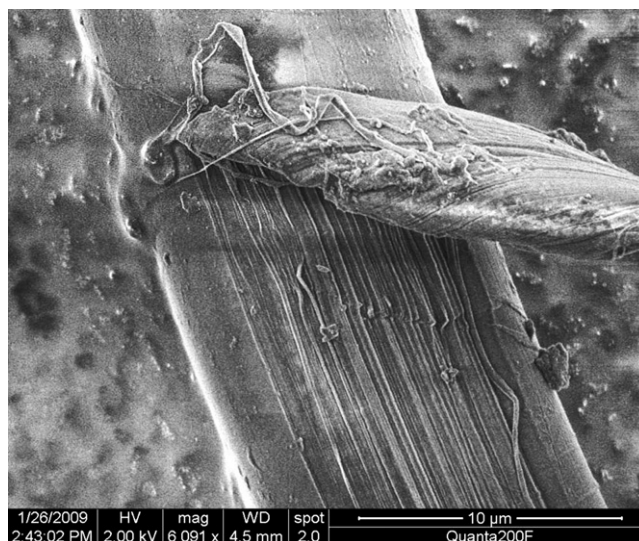


**Fig. B.11.** Electron micrograph showing the fibrillar structure underneath the delaminated surface of a single as spun PPTA filament.

increase in orientation as observed by Ran et al. [13]. Excluding that, the integrated intensity underneath a scattering curve is proportional to  $V_{\text{irr}}\nu_1\nu_2(\rho_1-\rho_2)^2$ , where  $V_{\text{irr}}$  is the irradiated sample volume,  $\nu_1$  and  $\rho_1$  are the volume fractions and the electron densities of the contrasting phases, respectively. A significant increase in scattering must be caused either by a change in volume fraction (when the volume fractions are not close to  $\nu_1 \approx \nu_2 \approx 0.5$ ) or through a change in electron density contrast. This implies that for these loops, we may either have an increase in the volume fraction of voids (as cracks, slip planes or gaps between buckled fibrils), or that moisture is forced out of voids and thereby increasing the contrast, or a combination of both. This implies that we cannot analyse the total scattered intensity to retrieve the volume of the scatterers without more knowledge of the void content. With the filaments placed in air during the measurement, it is possible that moisture enters some voids accessible from the surface [8]. This

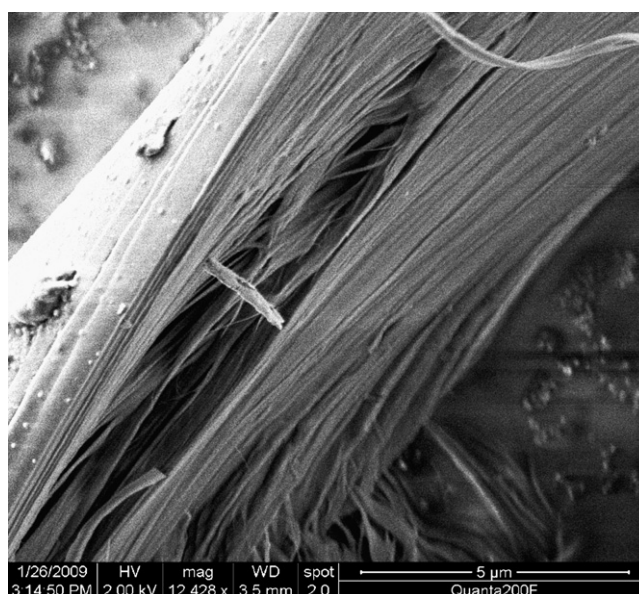


**Fig. B.12.** Electron micrograph showing the fibrillar structure underneath the surface of a cut single filament of as spun PPTA. Note in particular the presence of stacked tape-like fibrils, which are the subject of the subsequent SAXS measurements.

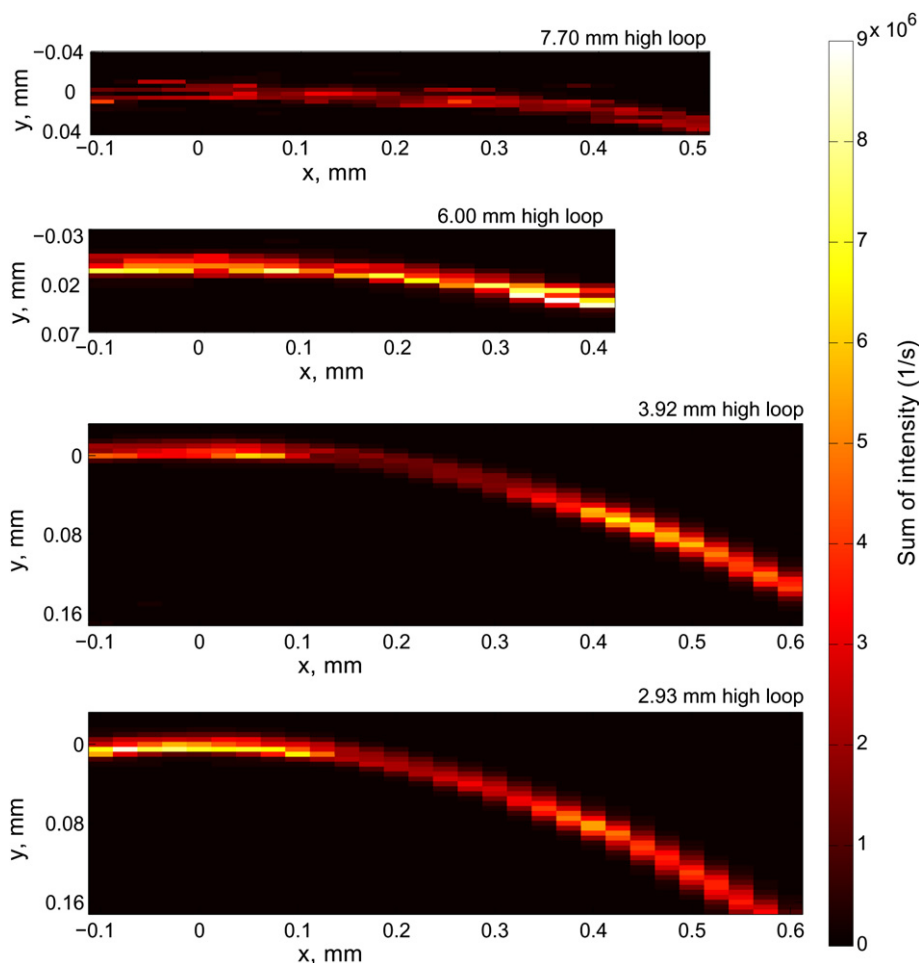


**Fig. C.13.** Intensity maps, colour axis units in counts per second integrated over the extracted 1D plots. It is readily seen that the radius of curvature decreases when reducing the loop size (top to bottom), accompanied by an increase of the scattered intensity. (For interpretation of the references to colour in this figure legend, the reader is referred to the web version of this article.)

will have an effect on the scattered intensity, lowering the contrast between polymer and voids. The intensity scattered from samples with moisture-filled voids is estimated to be approximately 25% that of empty voids by density considerations. It is furthermore not known what effect strain has on the moisture content of these fibres, as it may result in mechanical drying as for example observed with spider silk [30].

Analysis of the rotation angle of the main line of intensity of the scattering pattern demonstrates that the main scattering pattern axis is always perpendicular to the filament for all observed loop sizes. Analysis of this rotation behaviour enables the calculation of the radius of curvature. The equation  $e = r/R_m$  yields the compressive strain (and tensile strain) for filaments with a radius  $r$  [15],  $R_m$  being the radius of curvature at the apex of the loop. The radii of curvature determined for our four loop sizes are 2.97, 2.27, 1.43 and 1.05 mm, corresponding to strain values of 0.0040, 0.0053, 0.0084 and 0.0110, i.e. around published values for PPTA fibre critical compression strains of 0.006–0.008 [15]. Reversibility of the loop-induced strain effects has not been investigated.

## References

- [1] Northolt MG, Sikkema DJ. Lyotropic main chain liquid crystal polymers. *Advances in Polymer Science* 1991;98:119–72.
- [2] Ruland W. Carbon fibers. *Advanced Materials* 1990;2(11):528–36.
- [3] Effler LJ, Fellers JF. Structural orientation functions for anisotropic small-angle scattering. *Journal of Physics D* 1992;22:74–8.
- [4] Jiang H, Adams WW, Eby RK. High performance polymer fibres: material science and technology (a comprehensive treatment), vol. 12. VCH; 1993 [chapter 13].
- [5] Sawyer LC, Chen RT, Jamieson MG, Musselman IH, Russell PE. The fibrillar hierarchy in liquid crystalline polymers. *Journal of Materials Science* 1993;28:225–38.
- [6] Mooney DA, MacElroy JMD. Differential water sorption studies on kevlar 49 and as-polymerised poly(*p*-phenylene terephthalamide): adsorption and desorption isotherms. *Chemical Engineering Science* 2004;59:2159–70.
- [7] Aerts J. Small-angle X-ray scattering of aramid fibre. *Journal of Applied Crystallography* 1991;24:709–11.
- [8] Saijo K, Arimoto O, Hashimoto T, Fukuda M, Kawai H. Moisture sorption mechanism of aromatic polyamide fibres: diffusion of moisture into regular kevlar as observed by small-angle X-ray scattering technique. *Polymer* 1994;35:496–503.
- [9] Pauw BR, Vigild ME, Mortensen K, Andreasen JW, Klop EA. Analysing the nanoporous structure of aramid fibres. *Journal of Applied Crystallography* 2010;43:837–49.
- [10] Chae HG, Kumar S. Rigid-rod polymeric fibers. *Journal of Polymer Science: Applied Polymer Symposium* 2006;100(1):791–802.
- [11] Dobb MG, Johnson DJ, Majeed A, Saville BP. Microvoids in aramid-type fibrous polymers. *Polymer* 1979;20:1284–8.
- [12] Dobb MG, Johnson DJ, Saville BP. Direct observation of structure in high-modulus aromatic fibers. *Journal of Polymer Science: Polymer Symposium* 1977;58:237–51.
- [13] Ran S, Fang D, Zong X, Hsiao BS, Chu B, Cunniff PM. Structural changes during deformation of kevlar fibers via on-line synchrotron saxs/waxsd techniques. *Polymer* 2001;42:1601–12.
- [14] Grubb DT, Prasad K, Adams WW. Small-angle x-ray diffraction of kevlar using synchrotron radiation. *Polymer* 1991;32(7):1167–72.
- [15] Fidan S, Palazotto A, Tsai CT, Kumar S. Compressive properties of high-performance polymeric fibers. *Composites Science and Technology* 1993;49:291–7.
- [16] Dobb MG, Johnson DJ, Saville BP. Compressional behaviour of kevlar fibres. *Polymer* 1981;22:960–5.

- [17] Dobb MG, Robson RM. Structural characteristics of aramid fibre variants. *Journal of Materials Science* 1990;25:459–64.
- [18] Andrews MC, Lu D, Young RJ. Compressive properties of aramid fibres. *Polymer* 1997;38:2379–88.
- [19] Loidl D, Paris O, Burghammer M, Riekel C, Peterlik H. Direct observation of nanocrystallite buckling in carbon fibers under bending load. *Physical Review Letters* 2005;95: 225501–1–225501–4.
- [20] Eikenberry EF, Brönnimann C, Hülsen G, Toyokawa H, Horisberger R, Schmitt B, et al. Pilatus: a two-dimensional X-ray detector for macromolecular crystallography. *Nuclear Instruments and Methods in Physics Research A* 2003;501:260–6.
- [21] Jackson CL, Schadt RJ, Gardner KH, Chase DB, Allen SR, Gabara V, et al. Dynamic structure and aqueous accessibility of poly(*p*-phenylene terephthalamide) crystallites. *Polymer* 1994;35(6):1123–31.
- [22] Oster G, Riley DP. Scattering from cylindrically symmetric systems. *Acta Crystallographica* 1952;5:272–6.
- [23] Greenwood JH, Rose PG. Compressive behaviour of kevlar 49 fibres and composites. *Journal of Materials Science* 1974;9:1809–14.
- [24] Li LS, Allard LF, Bigelow WC. On the morphology of aromatic polyamide fibres (kevlar, kevlar-49, and prd-49). *Journal of Macromolecular Science, Part B* 1983;22:269–90.
- [25] Davies RJ, Koenig C, Burghammer M, Riekel C. On-axis microbeam wide- and small-angle scattering experiments of a sectioned ppta fiber. *Applied Physics Letters* 2008;92: 101903–1–101903–3.
- [26] Yabuki K, Ito H, Oota T. Consideration on the relation between fine structure and mechanical properties of poly(*p*-phenylene terephthalamide) fibers. *Sen-i Gakkaishi* 1976;32:T55–61.
- [27] Gaymans RJ, Tijssen J, Harkema S, Bantjes A. Elastic modulus in the crystalline region of poly(*p*-phenylene terephthalamide). *Polymer* 1976;17:517–8.
- [28] Stribeck N. X-ray scattering of soft matter. Berlin Heidelberg: Springer-Verlag; 2007.
- [29] Schmidt-Rohr K. Simulation of small-angle scattering curves by numerical fourier transformation. *Journal of Applied Crystallography* 2007;40:16–25.
- [30] Riekel C, Vollrath F. Spider silk fibre extrusion: combined wide- and small-angle X-ray microdiffraction experiments. *International Journal of Biological Macromolecules* 2001;29:203–10.